ADVANCED MATERIALS
www.advmat.de

Development of Bio-Voltage Operated Humidity-Sensory Neurons Comprising Self-Assembled Peptide Memristors

*Ziyu Lv, Shirui Zhu, Yan Wang, Yanyun Ren, Mingtao Luo, Hanning Wang, Guohua Zhang, Yongbiao Zhai, Shilong Zhao, Ye Zhou, Minghao Jiang, Yan-Bing Leng, and Su-Ting Han**

Biomimetic humidity sensors offer a low-power approach for respiratory monitoring in early lung-disease diagnosis. However, balancing miniaturization and energy efficiency remains challenging. This study addresses this issue by introducing a bioinspired humidity-sensing neuron comprising a self-assembled peptide nanowire (NW) memristor with unique proton-coupled ion transport. The proposed neuron shows a low Ag^+ activation energy owing to the NW and redox activity of the tyrosine (Tyr)-rich peptide in the system, facilitating ultralow electric-field–driven threshold switching and a high energy efficiency. Additionally, Ag^+ migration in the system can be controlled by a proton source owing to the hydrophilic nature of the phenolic hydroxyl group in Tyr, enabling the humidity-based control of the conductance state of the memristor. Furthermore, a memristor-based neuromorphic perception neuron that can encode humidity signals into spikes is proposed. The spiking characteristics of this neuron can be modulated to emulate the strength-modulated spike-frequency characteristics of biological neurons. A three-layer spiking neural network with input neurons comprising these highly tunable humidity perception neurons shows an accuracy of 92.68% in lung-disease diagnosis. This study paves the way for developing bioinspired self-assembly strategies to construct neuromorphic perception systems, bridging the gap between artificial and biological sensing and processing paradigms.

1. Introduction

Humidity measurement is one of the most reliable, precise, and secure methods for biometric identification.[1–3] Humidity identification offers unique advantages compared with conventional biometric modalities, such as fingerprints, iris, face, and DNA, which require user cooperation. Continuous, noninvasive transcutaneous evaporation creates a dynamic microclimate that reflects the internal physiology[4]; this readily accessible biomarker exhibits high potential for real-time health monitoring through sensitive, miniaturized humidity sensors. Studies on downstream processing have explored the application of humidity recognition systems in diverse real-world scenarios.[5,6] Humidity recognition technology is currently applied in healthcare settings to monitor and assess the respiration parameters of an individual, including rhythm, frequency, and tidal volume, for the early detection of pulmonary diseases (i.e., asthma and restrictive lung diseases) and prevention of respiratory

Z. Lv, M. Luo, H. Wang, G. Zhang, Y. Zhai, M. Jiang
College of Electronics and Information Engineering
Shenzhen University
Shenzhen 518060, P. R. China

S. Zhu, Y.-B. Leng
Institute of Microscale Optoelectronics
Shenzhen University
Shenzhen 518060, P. R. China

Y. Wang
School of Microelectronics
Hefei University of Technology
Hefei 230009, P. R. China

Y. Ren
2020 X-Lab
Shanghai Institute of Microsystem and Information Technology
Chinese Academy of Sciences
Shanghai 200050, China

S. Zhao
School of Electronic Information Engineering
Foshan University
Foshan 528000, P. R. China

Y. Zhou
Institute for Advanced Study
Shenzhen University
Shenzhen 518060, P. R. China

S.-T. Han
Department of Applied Biology and Chemical Technology
The Hong Kong Polytechnic University
Kowloon, Hong Kong 999077, P. R. China
E-mail: suting.han@polyu.edu.hk

The ORCID identification number(s) for the author(s) of this article can be found under https://doi.org/10.1002/adma.202405145

DOI: 10.1002/adma.202405145

failure.[7] For example, dyspnea in symptomatic asthma, which results from significant airway narrowing (600% increase in resistance), is often accompanied by wheezing[8] as patients compensate for the increased tidal volume to maintain minute ventilation. Conversely, in restrictive lung diseases with limited lung volumes, an increased respiratory rate becomes the primary compensatory mechanism owing to a shortened time constant. Thus, the contrasting pathophysiology of obstructive and restrictive disorders dictates distinct respiratory responses to maintain gas exchange during symptomatic episodes.

However, conventional humidity sensing systems rely on separate sensors for analog data acquisition[9] and require analog-to-digital conversion, data storage, and processing units, resulting in limited computing power and high energy consumption owing to extensive data transfer through limited bandwidth.[2,3] Such serial systems are constrained by bandwidth limitations that reduce their data processing efficiency, increase the total energy consumption, and involve security concerns. In contrast, biological sensory systems combine various senses that collaborate and connect with the brain, enabling the efficient perception and processing of real-world information. For humidity sensing, hygroreceptors in the human body receive humidity stimuli from the environment, which induce sensilla-structure shape changes that activate mechanosensitive molecules, resulting in the release of neurotransmitters to afferent neurons and electrical-spike conversion.[10,11] These spikes are subsequently sent to the cerebral cortex for further processing. This mechanism can be used as a template to develop a biological system integrated with extensive perception, preprocessing, and coding abilities. Intelligent devices that function as biologically inspired humidity-perception systems should be capable of simultaneously perceiving, filtering, memorizing, and processing humidity.[12–14] Additionally, these devices should preferably exhibit dynamic response under diverse humid environments with high sensitivity, a rapid response time, and long-term memory.[15–20] Considering the inherent digital characteristics and area inefficiency of CMOS hardware, several studies have identified memristive devices with analog multilevel resistance states, linear and symmetric switching characteristics, ultrafast switching, low power consumption, and high density as promising alternatives for implementing biologically inspired humidity perception systems.[21–25] Using material engineering and dynamic control, multimodal memristors can be developed to concurrently detect, memorize, and process humidity sensory signals.[26] Moreover, the matrix vector can be multiplied in a single clock cycle by assembling the cumulative output conductance of the memristive cells in crossbar arrays and using Ohm's and Kirchhoff's laws,[27,28] facilitating highly parallel arithmetic with low latency and power consumption.[29–31] However, two-terminal memristors show certain nonideal device characteristics[32] that limit their application in biologically inspired humidity perception systems. First, such systems show low sensitivity to humidity as the ion migration dynamics inside the switching layer are difficult to control via the proton source on varying the relative humidity (RH). This challenge can be addressed by integrating highly hydrophilic materials (such as materials with abundant —OH groups or open metal sites) as switching layers in such systems. These materials enhance water-molecule adsorption/desorption and promote the formation of well-defined protonation pathways, enabling the precise modulation of proton-coupled ion transport and, consequently, the electronic response of the memristor under varying humidity conditions. Second, the significant difference between the energy efficiency of memristors and their biological counterparts (≈20 watts for the brain) hinders the commercialization of large-scale chips for practical application. With the advent of the AI era, the exponential growth in data-centric computational tasks has imposed stringent requirements on the energy efficiency of neuromorphic perception systems.[33,34] Third, memristors show simple computing capability with less faithful biological features. Most two-terminal memristors exhibit first-order behavior with a single variable and are only capable of low-complexity programmable computing. This limitation can be overcome by manipulating the electro-physicochemical processes in the switching material in memristors with multiple variables to facilitate the imitation of a biomimetic performance with higher-order complexity.[35]

Proton-mediated signaling combined with neurotransmitters has been discovered mostly in sensory neurons in conditioned learning, indicating that integrating a proton-coupled ion migration mechanism in memristors is a key factor in designing biologically inspired humidity perception systems.[36–38] Several recently developed bioinspired peptide semiconductors that exhibit a wide range of supramolecular morphologies with diverse optical and electrical properties have been investigated for potential non-biomedical applications in diverse systems including field-effect transistors, capacitors, memories, Schottky diodes, ferroelectric-related devices, and logic gate systems.[39] Short peptides with aromatic amino acids can undergo self-assembly to form disparate supramolecular structures that exhibit kinetic or thermodynamic stability.[40] Diverse assembly approaches can be used to establish functional elements and nano-structural arrays with equally tunable morphologies and manipulated semiconducting characteristics.[41] Well-defined and directional intermolecular interactions (such as hydrogen bonding and aromatic π–π interactions) coupled with the facile chemical modification of peptides and their derivatives could be utilized to readily regulate and functionalize the electrical characteristics of peptide self-assemblies for diverse applications.[42]

Previous reports indicate that protons can locally accumulate on electrically insulating peptide films, facilitating metal redox reactions. A paper published in 2021 reports an electrochemical metallization (ECM)-based memristor (Ag/diphenylalanine/Ag) that exhibits short-term memory features with repeatable relaxation dynamics and a low temporal variation (σ/μ) of 0.09, confirming that a self-assembling structure comprising peptide–diphenylalanine nanowire can confine the migration of Ag^+ ions and the formation/rupture of conductive Ag filaments.[41]

In this study, we report a humidity sensory neuron based on a self-assembled cyclo(-Tyr-Tyr) nanowire (c-YY NW); c-YY is a cyclic dipeptide consisting of two tyrosine (Tyr) memristors exhibiting unique proton-coupled ion diffusion dynamics. The crystalline nanostructure of the peptide nanowire combined with the redox activity of the Tyr-rich peptide (cyclo(-Tyr-Tyr)) results in a significantly low Ag^+-migration activation energy in the proposed system, facilitating ultralow electric-field–driven threshold switching (≤0.1 V) and high energy efficiency (energy consumption per set event: 750 fJ). Additionally, the dynamics of Ag^+ migration can be controlled via a proton source owing to the hydrophilic nature of the phenolic hydroxyl group of tyrosine,

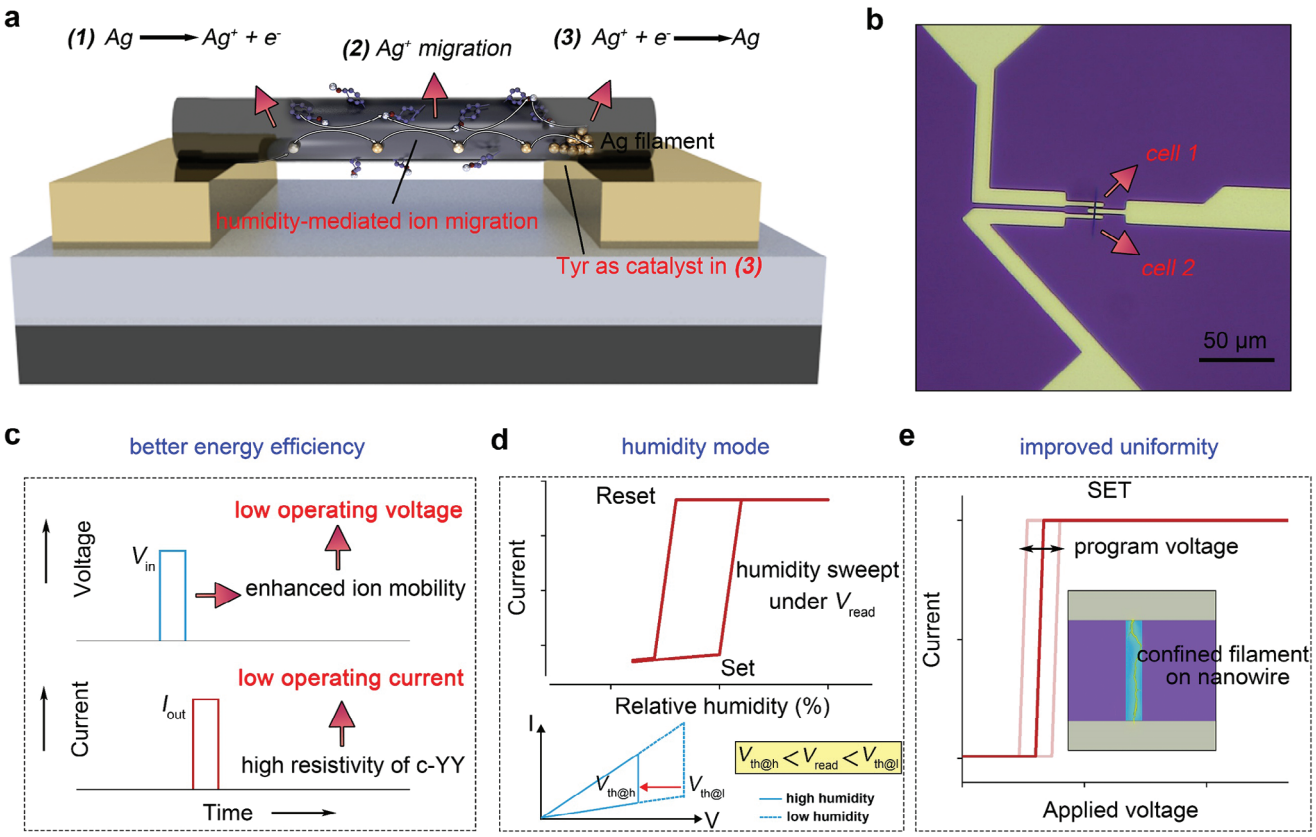

Figure 1. Multi-factor peptide-based memristors proposed in this study. a) Schematics of Tyr-Try peptide nanowires (c-YY NW) that 2) facilitate a humidity-related Ag^+ migration process and 3) lower the activation barrier of Ag^+ reduction, facilitating a humidity mode and a decrease in the V_{set}. b) Device image of two Ag/c-YY NW/Ag memristors (denoted as cell 1 and cell 2). Electrode spacing: 2 μm, scale bar: 50 μm. Schematics of the c) high energy efficiency, d) humidity mode, showing the processing of memristors by a humidity sweep under V_{read} ($V_{th@h}/V_{th@l}$ is the threshold voltage at a high/low humidity range), and e) good uniformity that are simultaneously shown by the multi-factor peptide-based memristors proposed in this study.

providing an effective strategy to control the conductance state of the memristor by changing the RH of the environment. Based on this operating principle, a neuromorphic perception neuron comprising a self-assembled peptide nanowire memristor that can encode humidity signals into spikes was developed in this study.[43] The spiking characteristics (i.e., firing frequency and amplitude of the output voltage) of the humidity perception neuron could be efficiently modulated, ensuring an emulation of the strength-modulated spike frequency characteristics of biological neurons. Owing to efficient tunability, these humidity perception neurons could be incorporated into a three-layer spiking neural network, which showed an accuracy of 92.68% for lung-disease diagnosis (asthma and restrictive lung disease), as input neurons. Thus, the peptide-based memristive hardware developed in this study exhibits significant potential as a neuromorphic sensory systems.

2. Device Concept

The c-YY NW-based memristive cells were fabricated by bridging a pair of Ag electrodes with isolated c-YY on a pre-cleaned SiO_2 substrate. A schematic diagram and optical image of the c-YY NW-based memristor are shown in **Figure 1**a,b (see Experimental Section, Figure S1, Supporting Information, for fabrication details). Individual NW memristors were fabricated by the dry transfer of c-YY NWs onto pre-patterned electrodes (Cr/Ag: 5/50 nm) with a spacing of 2 μm. The switching dynamics in such Ag active electrode-based ECM memories typically comprise the following three steps (Figure 1a): first, the oxidation of an active anode material ($Ag \rightarrow Ag^+$); second, Ag^+ migration; and third, cathodic reduction ($Ag^+ + e^- \rightarrow Ag$).[44] In this study, c-YY NW was used as the switching layer of a planar-structured memristor to regulate this three-step ECM process and develop a system with specific humidity-mediated switching characteristics. The developed system showed good energy efficiency (Figure 1c) owing to the Tyr in c-YY NW, which showed high proton conductivity and redox activity, facilitating the reduction and movement of Ag^+ on c-YY NWs, lowering the switching voltage of the device (Figure 1a). In conjunction with both the low OFF-state current (due to the low conductivity of c-YY NW) and ON-state current (controlled by the compliance setting), the energy efficiency of the c-YY NW-based memory cells could be significantly improved.[45,46] The proposed system also showed humidity-mediated switching behavior (Figure 1d). A greater number of water molecules were adsorbed on the NW surface under high-humidity conditions, leading to a higher concentration of hydroxyl radicals at the negative electrode. This induced a concomitant increase in the Ag^+ concentration at the anode to

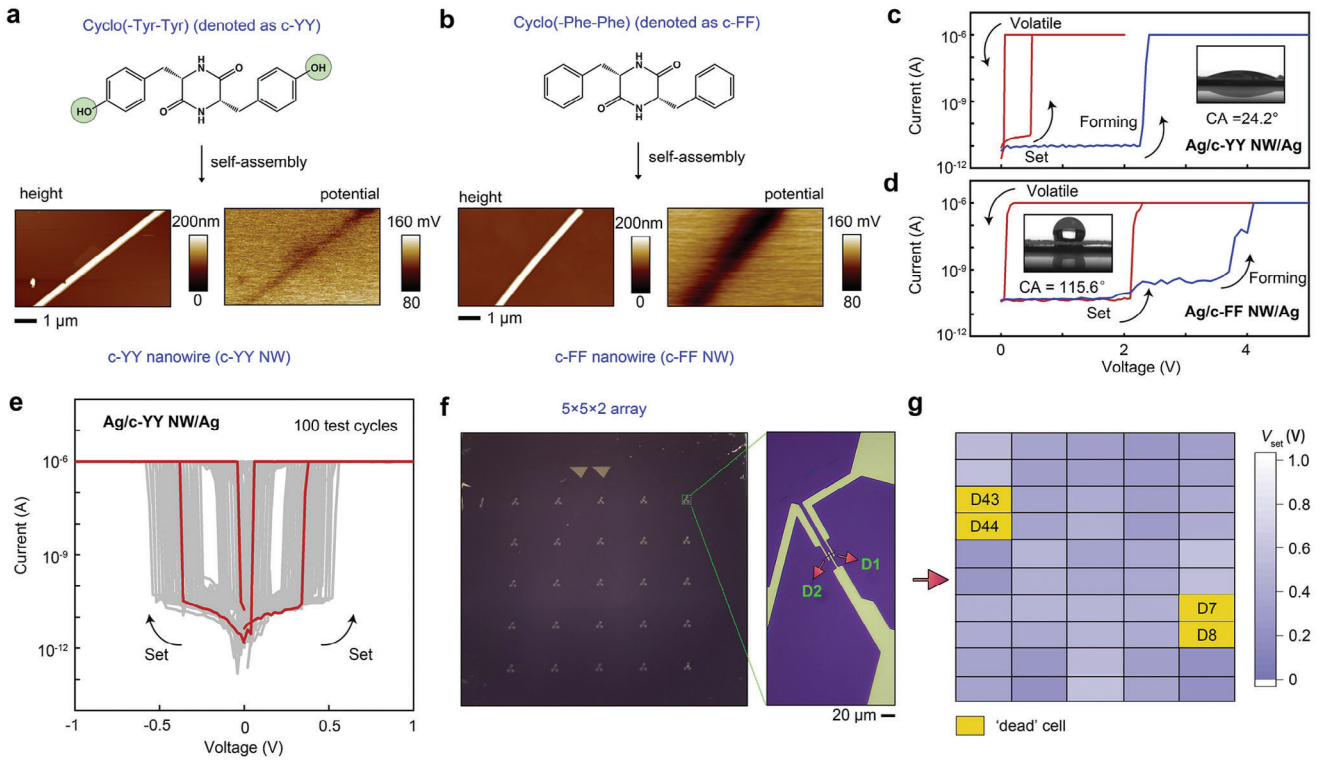

Figure 2. Threshold switching behavior and statistics. Chemical structures (top panel) of a) cyclo(-Tyr-Tyr) (labeled c-YY) and b) cyclo(-Phe-Phe) (labeled c-FF), and AFM (bottom panel; left) and KPFM (bottom panel; right) images of the corresponding self-assembling nanowires (NWs). Forming and resistive switching features of c) Ag/c-YY NW/Ag and d) Ag/c-FF NW/Ag (electrode spacing: 2 μm). Compliance current: 1 μA. Inset: water contact angle of c-YY and c-FF NW films. e) Repeatable memristive switching behavior of the Ag/c-YY NW/Ag cell under a positive and negative sweep. f) Optical image of a 5 × 5 × 2 Ag/c-YY NW/Ag memristor array and a zoom-in image of devices 1 and 2 (scale bar: 20 μm). g) Average V_{set} of the memristor array (see Figure S7, Supporting Information, for *I–V* curves of each cell). "Dead" cell (marked by yellow boxes) indicates the cells that cannot be formed.

maintain electrical neutrality. Furthermore, the enhanced proton concentration promoted the rapid migration of Ag ions.[47] Therefore, humidity variations induced changes in the structure (i.e., the orientation of functional groups) and electrical-property alterations in hydrophilic self-assembled c-YY NWs (Figure S2a, Supporting Information), affecting the filament growth dynamics and imparting humidity-mediated switching properties to the as-developed c-YY NW-based memristors.[35,48] Figure 1d shows that the as-developed device can be turned on and off by a humidity sweep (low → high → low humidity) at an appropriate reading voltage. The threshold voltage of the device decreases significantly with increasing humidity, reducing below the value of the reading voltage; this turns on the device. Notably, the proposed device showed excellent switching uniformity (Figure 1e), possibly because the c-YY NWs with high crystallinity provide a preferential ion-migration channel, confining the metallic filament growth in 1D nanostructures and consequently enhancing the cycle-to-cycle uniformity of the device.[49,50]

3. Proton-Activated Memristor

To analyze the synergistic effect of redox-active groups in c-YY NWs, devices based on c-YY NW with additional phenolic hydroxyl groups on cyclo(-Tyr-Tyr) and a control device based on cyclic diphenylalanine nanowires (labeled c-FF NW) were fabricated; mobile Ag ions from active Ag electrodes and protons from the atmosphere resulted in the resistive switching reported here. Notably, cyclo(-Phe-Phe) is different from other molecules in the presence of additional phenolic hydroxyl groups on c-YY (**Figure 2a**, green circles), which impart the entire system with redox properties. Here, c-YY and c-FF NWs with similar dimensions (≈500 nm) were fabricated via a bottom-up method for constructing memristive cells by precisely adjusting the ratio of 1,1,1,3,3,3-hexafluoro-2-propanol to H_2O.[51] Atomic force microscopy (AFM) and Kelvin probe force microscopy (KPFM) images (Figure 2a,b) indicate that the as-synthesized c-YY and c-FF NWs exhibit similar sizes but different surface potentials. X-ray diffraction measurements indicate that the dense packing of c-YY molecules ensure the self-assembly of c-YY NWs with good crystallinity (Figure S3a, Supporting Information) and hydrophilicity, while thermogravimetric analysis (Figure S3b, Supporting Information) indicates that the hydrophilic c-YY NWs comprise monohydrate units consisting of one cyclo(-Tyr-Tyr) molecule and one H_2O molecule, consistent with the results of previous studies.[52]

Single c-YY and c-FF NW-based memristive cells were fabricated by bridging a pair of Ag electrodes with isolated c-YY or c-FF NWs on a pre-cleaned SiO_2 substrate. A schematic diagram and an optical image of the c-YY NW-based memristor are shown in Figure 1a,b; the fabrication details are provided in Experimental Section, Figure S1 (Supporting Information). Initially, both the Ag/c-YY and Ag/c-FF NW/Ag cells were insulating (i.e., in a high-resistance state, HRS); thus, electroforming was required to

create conductive filaments. By varying the applied voltage from 0 to 5 to 0 V, the Ag/c-YY NW/Ag and Ag/c-FF NW/Ag cells could be switched from the HRS to a low-resistance state (LRS) at 2 and 4 V, respectively (Figure 2c,d). Both the c-YY and c-FF NW memristors spontaneously relaxed back to the HRS when the applied voltage was lower than the holding voltage, indicating threshold switching characteristics.[53] After electroforming, the c-YY NW-based device exhibited transient switching with a low V_{set} of 0.4 V, a high switching current ratio (>10^4), and a steep turn-on slope (<5 mV dec^{-1}) under a compliance current of 1 µA. The high resistivity of c-YY NW (13.8 µS cm^{-1}, Figure S4, Supporting Information) indicates that device minimization can result in a lower V_{set} and ON-state current. Interestingly, the control device based on c-FF NWs exhibited a relatively large V_{set} (>2 V), indicating that the functional phenolic hydroxyl groups in c-YY facilitate the accelerated growth of Ag conductive filaments. The absence of switching behavior in Au/c-YY NW/Au (Figure S5, Supporting Information) and Ag/SiO_2/Ag devices, even under a high-voltage stress (25 V), highlights the importance of the synergistic effect of c-YY NW and Ag electrodes in ensuring the resistive switching functionality in the as-fabricated memristors.[54] Cyclic voltammetry indicated a low oxidation peak potential (Figure S6, Supporting Information), confirming the facile electron-donating ability of c-YY NWs, which facilitated the reduction of Ag ions and promoted the growth of metallic conductive filaments. These control experiments indicate that Ag-ion injection from the anode into the c-YY NW affects electron transport throughout the c-YY self-assembled structure. The injected Ag ions possibly coordinate with the functional groups within the peptide (i.e., —C═O) for Tyr-assisted reduction, thereby lowering the activation energy for cation injection and reduction.

To investigate the temporal/spatial switching uniformity, the cycle-to-cycle and device-to-device switching consistencies of the as-fabricated Ag/c-YY NW/Ag cells were studied. A one-by-one dry transfer approach with a polydimethylsiloxane (PDMS) stamp (≈1.2 × 1.2 mm^2) and an inter-electrode spacing of 3 mm was used to minimizes potential cross-contamination during 50-device array fabrication. Figure 2e shows 100 consecutive current–voltage (*I*–*V*) switching curves of a single cell in a 5 × 5 × 2 memristor array; the narrow distribution of the switching voltage indicates a good repeatability of the transient switching effect.[55] All 50 cells in the memristor array were used to evaluate the device yield (Figure 2f). The *I*–*V* switching curves of all 50 cells are shown in Figure 2e and Figure S7 (Supporting Information); 46 cells show similar volatile switching characteristics, while the remaining four cells show the HRS. The planar device showed a yield of 92% and device failure tended to occur simultaneously in pairs of devices sharing electrodes (such as D7, D8, D43, and D44), possibly owing to mechanical damage to the local c-YY NW nanostructure during the dry-transfer process. Figure S8 (Supporting Information) shows no device degradation over 1000 cycles (measured with pulses), indicating good device endurance and high potential for reliable implementation in neuromorphic computing tasks.

4. Humidity-Mediated Resistive Switching

Hydrophilic self-assembled c-YY NWs (inset of Figure 2c) exhibit high sensitivity to humidity stimuli because their functional-group orientation and assembly size, and their electrical behavior can be modulated by varying the RH instead of the electrical field. Molecular dynamics (MD) simulations indicate that the self-assembled nanostructures absorb a greater number of water molecules with increased sizes in both the axial and radial directions (Figure S9, Supporting Information) on increasing the RH. The adsorbed water molecules weaken the coordination effect between the Ag^+ and C═O groups, lowering the Ag^+ diffusion barrier. To verify the humidity-mediated switching effect of the proposed device further, the *I*–*V* characteristics of the c-YY NW memristor was investigated under different levels of RH (i.e., 15%, 30%, 45%, 60%, 75%, and 90%). The RH was easily controlled by injecting either humidified air or N_2 into the test chamber (**Figure 3a**). The V_{set} and switching speed could be tuned from 0.7 to 0.2 V and 11.36 to 0.05 s, respectively, by changing the RH level from 60% to 90% (Figure 3b,c).[56] Figure S10 (Supporting Information), shows the repeatable threshold switching of the fabricated device under different levels of RH (60%, 67.5%, 75%, 82.5%, and 90%). Notably, at 90% RH, the device remained in the LRS after the removal of the input voltage; the memristor completely recovered its initial state on exposure to a negative voltage sweep (compliance current: 10 mA, Figure S11a, Supporting Information) or a RH of 60% with a resting time of 15 s (Figure S11b, Supporting Information). A low value of V_{set} indicates that lower energy is required for the formation of conductive Ag filaments at higher levels of RH. At low levels of RH (i.e., 15%, 30%, and 45%), the devices showed a low-conductance state and could not be turned on after repeated SET operation for a prolonged duration, confirming the difficulty of inducing Ag filament growth under low RH levels. Interestingly, the resistive switching behavior of the Ag/c-YY NW/Ag device could be manipulated by RH alone, without the application of electrical stress (Figure 3d). The device was characterized by applying a constant voltage bias of 0.3 V and varying the RH level within 30–90%. The conductance of the device increased abruptly by four orders of magnitude at an RH level of ≈90%; this "humidity set" mode enabled the device to maintain the LRS for a prolonged period. Subsequently, on lowering the RH from 90% to 30%, the device first exhibited unstable behavior with transient fluctuations in conductance, and at an RH of ≈30%, the conductance of device abruptly decreased by three orders of magnitude. The decay time in conventional fading memory devices can be adjusted by manipulating the pulse duration, amplitude, and frequency.[57,58] The device fabricated in this study exhibited pulse-duration–dependent decay behavior, where the decay time increased from 8 to 47 ms as the pulse duration increased from 10 to 50 ms (at a pulse voltage with a constant amplitude of 1.5 V and a read voltage of 0.05 V). Notably, the decay time could be modulated by varying the humidity. To explore the effect of humidity on the filament-rupture process, the as-fabricated device was subjected to input pulses under different levels of RH (Figure 3f,g and Figure S12, Supporting Information). A step-like relaxation reduction was observed, which can be attributed to the interplay of two factors: the size-dependent stability of the conductive filaments and the low activation energy for Ag-ion migration in the c-YY NWs. Under high-humidity conditions, the formation of larger conductive filaments is favored because of enhanced Ag-ion migration, leading to a metastable period of the LRS (tens of

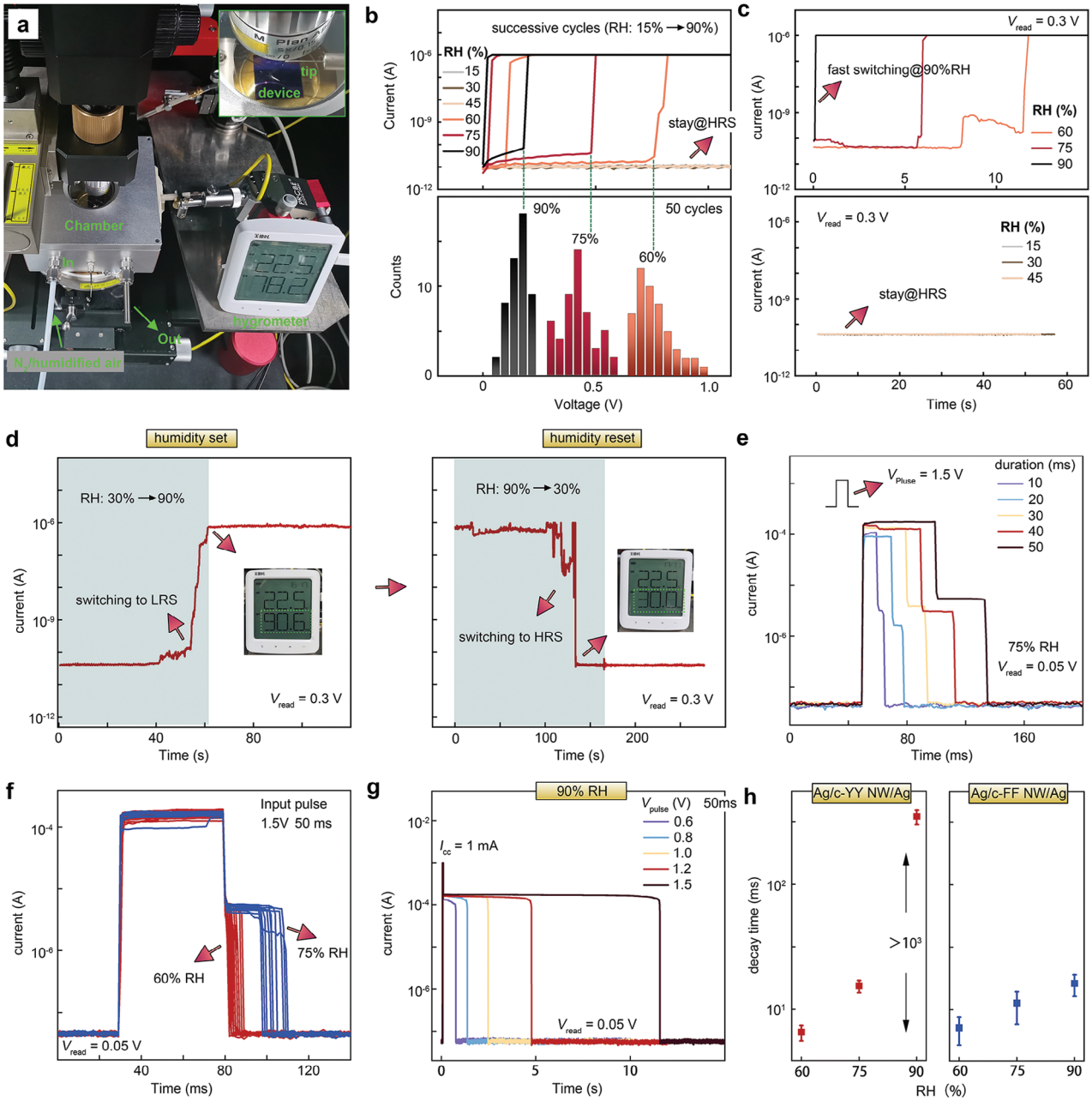

Figure 3. Humidity-mediated switching dynamics. a) Image of the probe station and probe chamber with humidity-control ability. N_2/humidified air is injected to modulate the relative humidity (RH) with an accuracy of ≈5% RH. b) *I–V* curves of the Ag/c-YY NW/Ag device under different RHs varying within 15–90% (top panel) and the V_{set} distribution of 50 cycles (at 60%, 75%, and 90% RH). A long interval between two subsequent cycles (10 s) is used to ensure a similar resting state. c) *I–t* curves measured at 0.3 V at RHs levels within 60–90% (top panel) and 15%–45% (bottom panel). d) Humidity set (left panel, RH changes from 30% to 90%, marked by gray rectangle) and humidity reset (right panel, RH changes from 90% to 30%, marked by a gray area) of an Ag/c-YY NW/Ag cell under the constant application of a read voltage of 0.3 V. e) Relaxation feature of the basic device in response to 1.5 V input pulses with durations within 10–50 ms (at 75% RH, V_{read} = 0.05 V). f) Relaxation feature of the basic device in response to f) 1.5 V/50 ms input pulses under 60% RH (red curves) and 75% RH (blue curves) and g) 50 ms input pulses (0.6, 0.8, 1.0, 1.2, and 1.5 V) under 90% RH. h) Decay times of Ag/c-YY NW/Ag (left panel) and Ag/c-FF NW/Ag (right panel) at different humidity levels.

milliseconds to several seconds) when the pulse voltage (1.5 V) switches to a read voltage (0.05 V), similar to a plateau. The rapid Ag migration in the c-YY NWs facilitates the rapid local destruction of the conductive filament (LRS to HRS) within a few milliseconds. This rapid transition occurs within a significantly shorter time period than the duration of the LRS plateau, leading to a step-like reduction in the conductance. To confirm this explanation, additional experiments were conducted with a lower current-compliance limit. Reducing the conductive-filament size led to a significant shortening of the LRS plateau,

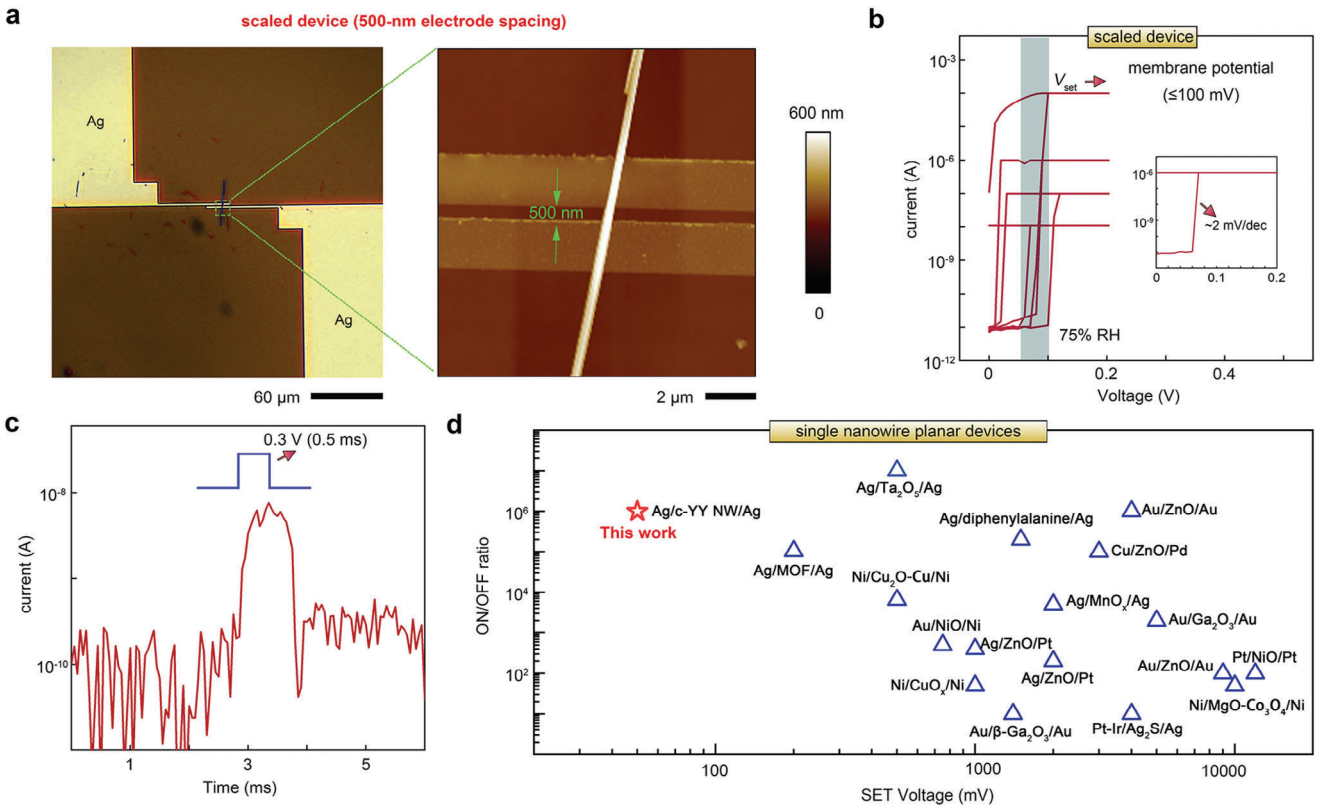

Figure 4. Threshold switching features of the scaled device and flexible Ag/c-YY NW/Ag device. a) Optical image and AFM image of a scaled Ag/c-YY NW/Ag device with an electrode spacing of 500 nm. Scale bars: 60 and 2 μm. b) Switching curves of the scaled device under different compliance currents at 75% RH. Inset: Magnified image of the switching curve; the turn-on slope is ≈2 mV dec^{-1}. c) Calculation of power consumption via pulse measurement with a set pulse (0.3 V/0.5 ms) at 75% RH. d) Comparison of the ON/OFF ratio and SET voltage of the scaled device developed in this study with some representative single NW planar memristors; the corresponding data is provided in Table S1 (Supporting Information).

ultimately resulting in the absence of a step-like conductance reduction (Figure S13, Supporting Information). The time required for the decay behavior spanned three orders of magnitude as the RH increased from 60% to 90%. Under high-humidity conditions, the formation of larger conductive filaments is favored because of enhanced Ag-ion migration, leading to a longer rupture process. This unique and extensive tunability of over three orders of magnitude opens up exciting possibilities for engineering Ag/c-YY NW/Ag devices with tailored decay characteristics for specific neuromorphic perception applications. Quantitative analysis indicated that higher humidity levels led to a significantly prolonged relaxation time (Figure 3h), confirming that the decay behavior of the Ag/c-YY NW/Ag device can be effectively tuned by modulating the RH. NW networks exhibit high potential for enhancing the humidity sensitivity of memristors because of their high surface area. However, incorporating NWs in memristors might necessitate a tradeoff between sensitivity and uniformity as controlling the conductive-filament growth in NW networks can be challenging. Compared with the hydrophilic c-YY NWs, humidity variations influenced the adsorbed-water content, proton concentration, and Ag-ion migration in c-FF NWs to a significantly lesser extent. This difference in material properties could explain the absence of humidity-dependent relaxation behavior in c-FF NW memristors (Figure S14, Supporting Information).

5. Scaled Device

Although the c-YY NW memristor exhibits reproducible and robust humidity-controlled threshold switching behavior, it exhibits switching voltage values that are higher than the recommendations of the International Technology Roadmap for Semiconductors for memristors. To address this energy efficiency issue, the c-YY NW memristor was scaled to smaller dimensions. **Figure 4a** shows the optical and AFM topographic images of the scaled memory cell with an electrode spacing of 500 nm. The scaled device exhibits a significantly lower V_{set} (50–100 mV) than previously reported nanowire planar devices (Figure 4b and Table S1, Supporting Information). At a fixed RH level of 75%, application of a voltage pulse with an amplitude of 0.3 V and duration of 0.5 ms abruptly flips the device state, resulting in a sharp switching slope of 2 mV per decade. Notably, the low OFF current (5 nA) of this device can be attributed to the inherently high electrical noise (0.5 nA) in the *I–V* parameter analyzer (Agilent B2902a). Figure 4d shows that the scaled Ag/c-YY NW/Ag device outperforms representative single-nanowire planar devices, exhibiting a better operating voltage, ON/OFF ratio, and energy consumption per switching event (750 fJ, Figure 4c). Therefore, the Ag/c-YY NW/Ag devices developed in this study exhibit high potential for practical application in low-power neuromorphic perception.

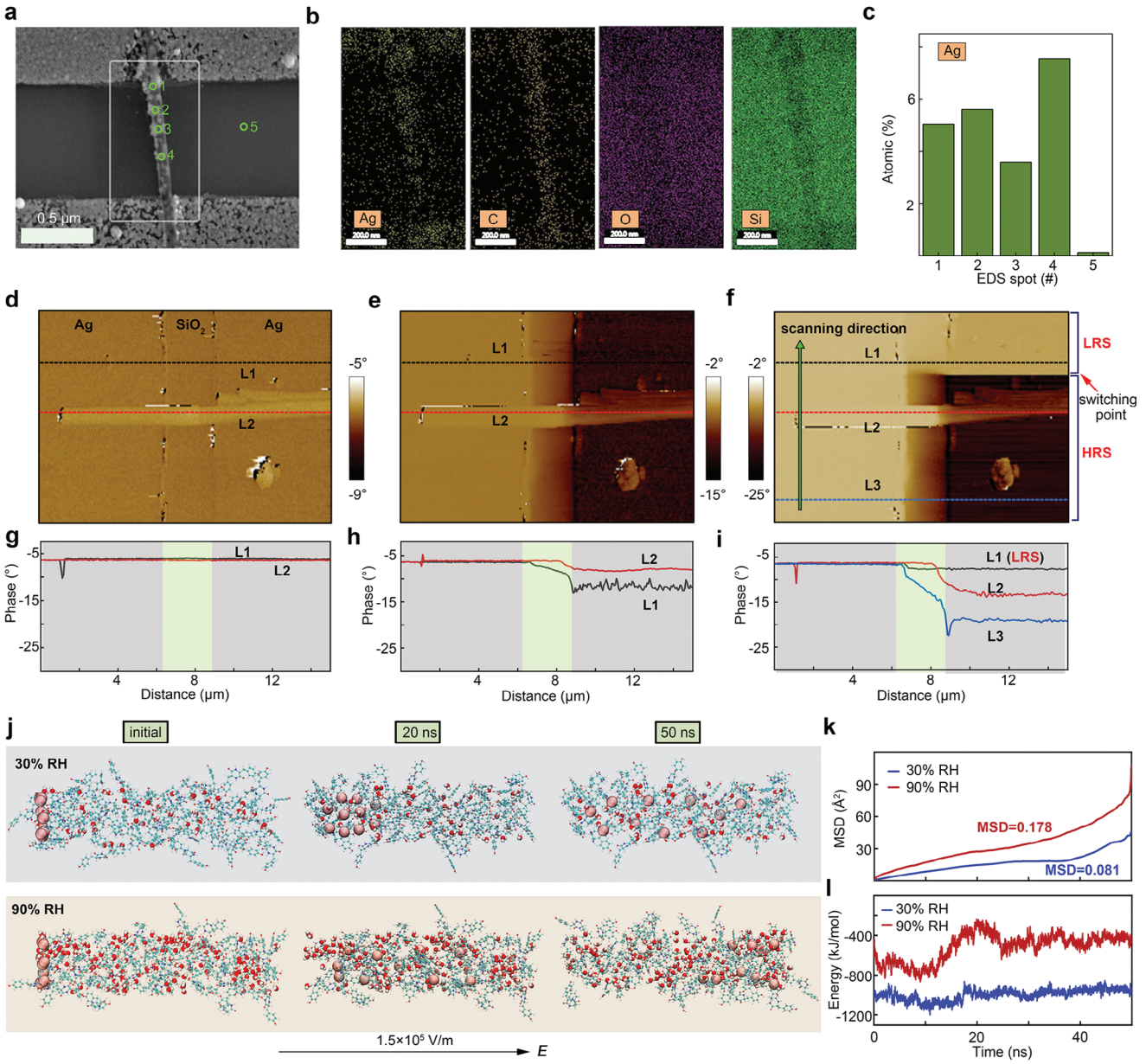

Figure 5. In situ SEM–EDS and EFM measurements of the switching process and the MD simulation results. a) SEM image of an Ag/c-YY NW/Ag device in an electroformed state. Scale bar: 0.5 μm. b) EDS mappings of Ag, C, O, and Si of the area marked by a rectangular box in (a). Scale bar: 200 nm. c) Ag atomic ratio (%) for the EDS spots 1–5 in (a). d,f) EFM images of the Ag/c-YY NW/Ag device at different input voltages (measured with a B2902A precision source/measure unit). d) $V_{input} = 0$ V (HRS); e) $V_{input} = 0.1$ V (HRS); and f) $V_{input} = 0.3$ V (bottom panel: HRS; top panel: LRS; scan direction from bottom to top). g–i) EFM phase profiles along the L1 (black), L2 (red), and L3 (blue) in (d–f). j) MD simulation of the mobility behavior (0, 20, and 50 ns) of Ag^+ in c-YY NWs at 30% (top panel) and 90% (bottom panel) RH. Applied field strength: 1.5×10^5 V m^{-1}. k) Mean square displacement (MSD) of Ag^+ versus time in c-YY NWs at 30% (blue) and 90% (red) RH. Applied field strength: 1.5×10^5 V m^{-1}. l) Binding energy between Ag^+ and c-YY NW at 30% (blue) and 90% (red) RH.

6. Proton-Mediated Switching Mechanism

The planar configuration of a memristor with a 1D switching medium facilitates the utilization of in situ techniques for probing switching mechanisms.[54] Here, scanning electron microscopy (SEM) and energy-dispersive X-ray spectroscopy (EDS) were used to confirm the formation of conductive Ag filaments during SET. After the SET operation, numerous nanoparticles were dispersed on the surface of the c-YY NW, whereas the SiO_2 surface remained relatively clear (**Figure 5a**). Furthermore, the EDS mapping of a selected region (marked by a white box) for Ag, C, O, and Si confirmed that the Ag nanoparticles were primarily located on the c-YY NW surface (Figure 5b). The quantitative analysis of the Ag atomic ratio in randomly selected areas (marked by green circles in Figure 5a) corroborated this finding. Locations 1–4 on the c-YY NW exhibited a significantly higher

Ag ratio than Location 5 on the SiO_2 surface (Figure 5c), confirming that the LRS of the Ag/c-YY NW/Ag device arises from Ag filamentary conduction, highlighting the crucial role of the c-YY NW in confining the location of filament growth. Subsequently, the dynamic switching behavior of the device was investigated using an atomic force microscope equipped with a Keysight B2902A parameter analyzer. The phase value during electric force microscopy (EFM) measurements, which exhibits high sensitivity to the ion behavior, is used to investigate ion migration, accumulation, and the subsequent formation of conducting filaments within filament-type memristors. The high spatial resolution (up to 10 nm) and charge-accumulation sensitivity of EFM make it particularly suitable for dynamic-process probing.[59] Figure 5d–f shows the EFM phase images recorded under different applied biases (0, 0.1, and 0.3 V). Initially, without an applied voltage, the c-YY NW and the two Ag electrodes exhibited similar phase values, indicating an initial-state device (Figure 5d). Notably, on applying a constant input voltage of 0.1 V (below the electroforming voltage), a distinct phase change (6°) was observed in the Ag anode (line 1, L1), while the memristor remained in the HRS (Figure S15a, Supporting Information). This result indicates significant contact resistance at the Ag/SiO_2 interface, which leads to charge accumulation near the anode region. In comparison, line 2 (L2), which bridges the two electrodes via the c-YY NW, exhibits a significantly smaller phase difference (1.5°), indicating that the c-YY NW shows a lower activation-energy barrier for Ag^+ migration, which facilitates ion-transport confinement along its surface. A comparison of the line profiles along L1 and L2 (Figure 5h) indicates that ion migration along the c-YY NW can reduce the phase difference between the anode and cathode. On stimulating the planar device with a higher voltage of 0.3 V (with a bottom-to-top scanning direction, Figure 5f), the device first stayed in an insulating state, inducing a relatively large phase difference (>12°) between the anode and cathode (the region does not cross the c-YY NW, marked by L3), indicating high charge accumulation (below the switching point, the device is in the HRS). Subsequently, the charge at the anode/NW interface migrated along the NW, resulting in a reduction of the phase difference (L2 in Figure 5i), and the device switched to the LRS (above the switching point, the device is in the LRS). The corresponding *I–t* curve is shown in Figure S15b (Supporting Information). Resistive switching occurred (marked by a red arrow) within the timeframe of one EFM-image experiment (i.e., within several minutes), leading to a negligible phase-value difference between the anode and cathode (L1 in Figure 5i).

MD simulations were used to elucidate the mechanism of humidity-mediated Ag^+-transport further.[60,61] In these simulations, the c-YY NWs were placed in 30% and 90% RH conditions. A significant increase in water absorption was observed on increasing the RH from 30% to 90%, resulting in a considerably higher H_2O/c-YY molar ratio. This increased water content facilitated the water reduction reaction at the cathode ($O_2 + H_2O + 2e^- \rightarrow 4OH^-$), which in turn promoted Ag ionization at the anode to maintain electroneutrality. The abundance of free Ag^+ ions facilitated the establishment of "stronger" conductive filaments with low susceptibility to fading. Additionally, the absorbed H_2O significantly affected the dimensions of the c-YY NW assembly. The simulation results (Figure S9, Supporting Information) indicate that the self-assembled cluster showed a larger size under 90% RH (length: 7.51 nm, diameter: 1.93 nm) than under 30% RH (length: 7.22 nm, diameter: 1.81 nm). The application of an electric field (1.5×10^5 V m^{-1}) at 90% RH induced the migration of oxidized Ag^+ ions along the surface of the pristine c-YY cluster axis, which reached the right side of the cluster within 50 ns (Figure 5j, bottom panel). Increasing the humidity triggered an increase in the Ag^+ concentration, facilitating the formation of a conductive filament through a positive-feedback process involving Ag^+ migration, resistance reduction, and temperature increment. In contrast, at 30% RH, the Ag^+ cations remained confined near the left side of the cluster, even after 20 ns of electrical stimulation, indicating hindered transport through the c-YY cluster, even on prolonged electric-field application (Figure 5j, top panel). The self-diffusion coefficients of c-YY NW were estimated to be 0.178 and 0.081 Å^2 ns^{-1} at 90% and 30% RH, respectively, confirming the higher transport efficiency of Ag^+ on c-YY NWs in higher RH conditions (Figure 5k). These simulation results are consistent with the experimental results of the humidity-accelerated switching behavior shown in Figure 3b,c. Furthermore, the interaction energy between the c-YY cluster and Ag^+ at 90% RH (-574.539 ± 169.181 kJ mol^{-1}) is significantly lower than that at 30% RH (-1028.682 ± 57.034 kJ mol^{-1}), unambiguously confirming humidity-accelerated Ag^+ migration within the c-YY cluster (Figure 5l). The humidity-dependent set/reset transition shown in Figure 3d can be explained as follows. An RH increment from 30% to 90% at a constant read voltage of 0.3 V induces device activation owing to the adsorption of water molecules, which exposes the phenolic hydroxyl functional groups on the peptide chains to the NW surface. These exposed groups function as chelating sites for Ag ions, expediting Ag^+ migration and the growth of conductive filaments, ultimately switching the device on.[39] Conversely, decreasing the RH from 90% to 30% may induce the structural collapse of c-YY NWs, resulting in the local rupture of the conductive filaments and a decrease in conductance.

7. Spike-Based Neuromorphic Perception System

Respiration, the exchange of gases between an organism and its surroundings, is an essential process in maintaining life. Abnormal respiration can indicate underlying physical problems. Many diseases, including heart disease, pulmonary disease, sleep apnea, and infection-related hyperpyrexia, can alter respiratory frequency and depth. Humidity sensing during respiratory monitoring is a promising approach for clinical diagnosis and treatment.[2] For example, asthmatics[8] show a normal breathing rate with an abnormally large tidal volume (i.e., each breath contains more water than normal), as shown in **Figure 6a**. In contrast, restrictive lung disease (68–72% RH) is characterized by a normal tidal volume and abnormally rapid breathing rate (i.e., humid gas is exhaled more frequently than normal). Therefore, a combination of humidity sensing and processing functions is expected to enable the efficient diagnosis of these pulmonary diseases. According to this hypothesis, a memristor was used to simultaneously sense and process humidity signals during respiration in this study. Figure 6b and Figure S16 (Supporting Information) show the humidity-perception neuron circuit developed in this study that leverages a c-YY NW memristor and an RC circuit to convert humidity signals into asynchronous

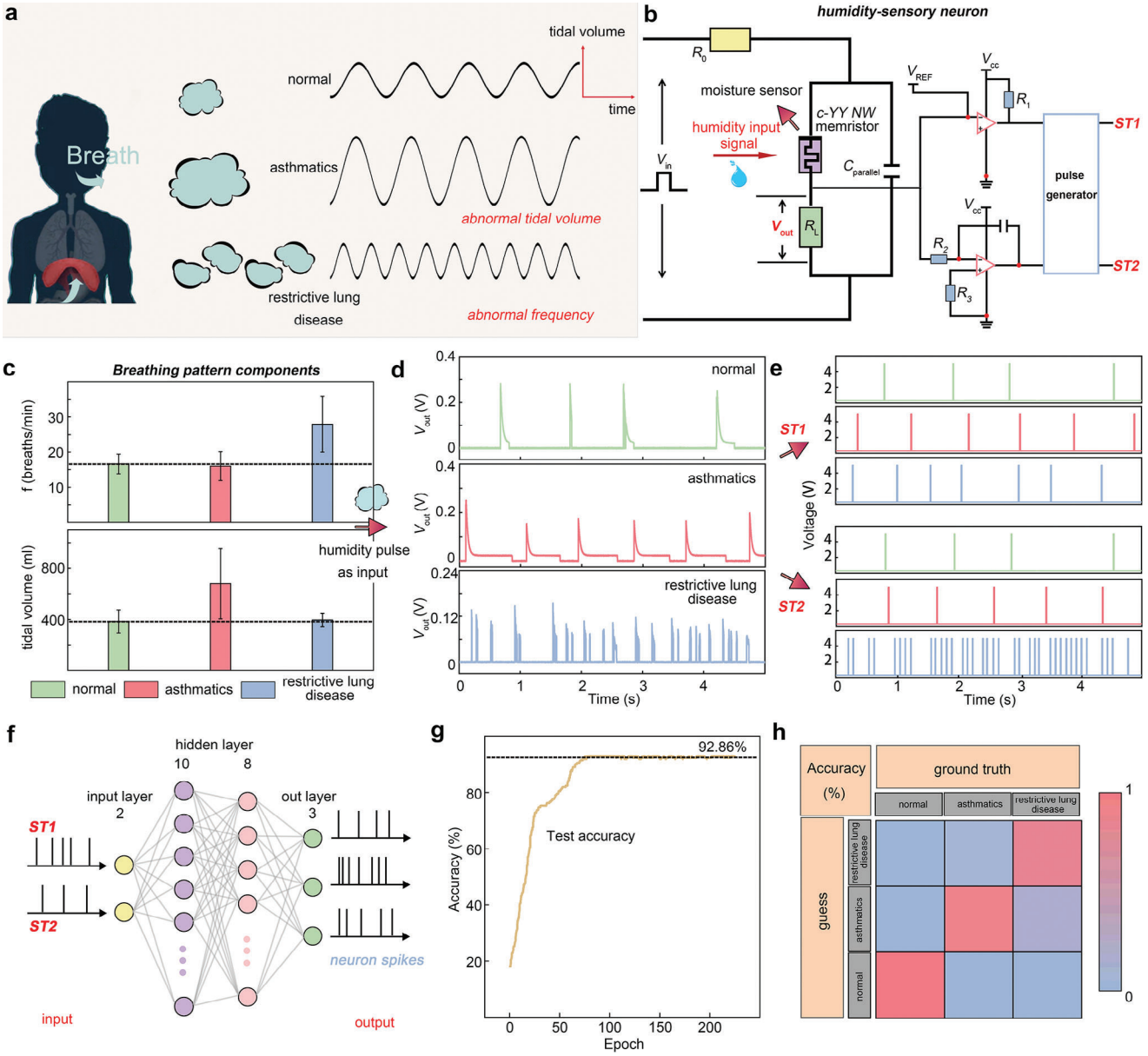

Figure 6. Illustration of the Ag/c-YY NW/Ag-based circuit for integrated sensing–processing functions. a) Schematics of the breathing patterns of a healthy individual (top panel), asthmatic (middle panel) individual, and patient with restrictive lung disease (bottom panel). b) Schematics of the as-developed artificial humidity-sensory neuron. The c-YY NW-based device functions as a moisture sensor with fading memory. V_{in} = 0.5 V, R_0 = 200 kΩ, R_L = 10 kΩ, $C_{parallel}$ = 3.3 μF. c) Breathing-pattern components (breathing frequency and tidal volume) of normal (green) and asthmatic (red) individuals along with those affected by restrictive lung disease (blue). d) Response of the artificial humidity-sensory neuron under different humidity-pulse stimulations. The humidity signals of normal individuals and those affected by asthma and restrictive ling disease are mimicked by adjusting the frequency of the humidity pulse and the pulse–memristor distance. e) Asynchronous ST1 and ST2 results under different humidity-pulse stimulations. f) Schematics of a three-layer artificial neural network for lung-disease classification. The fire frequency and V_{out} are extracted from (d). g) Classification accuracy as a function of training cycles. After 200 training epochs, the system shows a test accuracy of 92.86%. h) Confusion matrix showing the classification results. The occurrence probability of a predicted category is shown by the color bar in the figure.

spike trains. The circuit comprises a perception neuron, an intermediate amplifier, a comparator, and a signal generator. A load resistor (R_L, 10 kΩ) is connected in series with a c-YY NW memristor and in parallel with a capacitor ($C_{parallel}$, 3.3 μF). Under a stationary input voltage (V_{in}, 0.5 V), the voltage output (V_{out}) across R_L was monitored using an oscilloscope. Upon the application of V_{in}, $C_{parallel}$ begins to charge. When the voltage on $C_{parallel}$ reaches a critical threshold, the c-YY NW memristor switches to a high-conductivity state, generating a spike and discharging $C_{parallel}$ through R_L and the memristor.[62] As V_{out} decreases, the memristor resets, allowing the perception neuron to generate another spike upon subsequent charging with $C_{parallel}$. Therefore, two asynchronous spike trains (ST1 and ST2) are derived from V_{out}. The generation of the ST1 and ST2 pulses is dependent

on the comparator (LM393D) and differential circuit (LM358), respectively. The comparator triggers an output pulse when the input voltage exceeds the reference voltage of 0.1 V, while the differential circuit generates an output pulse when the input signal undergoes a step change from high to low. The outputs are converted into standard asynchronous spike trains (with an amplitude of 5 V) by a signal generator. Stimulation with RH levels within 64–85% induces a memristor resistance change from 10^{10} to 5×10^3 Ω, resulting in a wide range of resistance outputs. This effectively replaces R_L in the original neuron circuit, directly translating the humidity signal into the spiking frequency of the neuron.

Hence, the asynchronous spike encoder based on the c-YY NW memristor converts the humidity signals into two spike trains (ST1 and ST2). The breathing patterns (tidal volume and breathing rate) of three groups representing three types of breathing (normal, asthmatic, and restrictive lung disease), mimicked by a mini-humidifier, were used as humidity inputs to evoke humidity-sensory neurons. Notably, the humidity field does not directly trigger the switching behavior of the memristor. Instead, it modulates the threshold voltage of the memristor, which determines whether the applied voltage is sufficient to induce a resistance change. Under high-humidity conditions, the threshold voltage is reduced, enabling the memristor to switch at lower voltages. This characteristic of the memristor device developed in this study affects the charge/discharge behavior of the proposed neuron circuit. For normal breathing (64–73% RH), the neuron fires at a frequency of ≈0.8 Hz and shows a V_{out} of 0.22 V in response to an input voltage of 0.5 V and humidity (Figure 6d). With increasing tidal volume, as observed in asthmatics (80–85% RH), the frequency increases to ≈1.2 Hz and the V_{out} decreases to ≈0.17 V. This frequency increment can be attributed to humidity-mediated resistive switching. In the case of restrictive lung disease, an abnormal breathing rate of 27.9 breaths/min leads to a significant increase in the fire frequency (≈4.5 Hz), which is five times higher than that in healthy individuals. In this study, three distinct V_{out} values (Figure 6e) for the three studied groups were converted into asynchronous ST1 and ST2 signals, which were fed into a three-layer spiking neural network (SNN) for lung-disease diagnosis. Schematics of the spike-based neuromorphic perception system used for respiration monitoring is shown in Figure 6f. The SNN comprises an input layer with two nodes, two hidden layers with ten and eight nodes, respectively, and an output layer with three nodes. The asynchronous inputs were classified into three categories (normal, asthmatic, and restrictive lung disease) after training the network. Backpropagation, based on the experimentally measured electrical characteristics of the as-developed memristor and the dependence of the spiking frequencies and amplitudes of the humidity-sensory neural networks on the input humidity, was used for the online training of the SNN. Figure 6g shows the evolution of accuracy during training. The proposed network shows an accuracy of 92.68% after only 200 training iterations. Figure 6h shows a confusion matrix of the ground truth and guess for the classification of 210 test datasets. All three groups were classified correctly after 200 epochs (as indicated by the color bar), confirming the integrated sensing–processing ability of the proposed neuromorphic-sensing processing system.

8. Conclusion

In summary, this study introduces a novel biomimetic humidity-sensor neuron derived from a self-assembled cyclo(-Tyr-Tyr) nanowire memristor that exhibits unique proton-coupled ion-transport dynamics; the excellent performance of the proposed device can be attributed to the facile migration of Ag^+ ions along well-defined c-YY NWs. Notably, the memristors fabricated in this study show ultralow programming voltages (50–100 mV) and currents (10 nA) with a high ON/OFF ratio (>10^6) and device yield (92%). The phenolic hydroxyl group of Tyr functions as a proton source, affording excellent control over Ag^+ migration and the conductance state of the memristor in response to ambient humidity. Consequently, besides functioning as a sensitive humidity sensor, the proposed device exhibits high potential to facilitate the exploration of exciting new avenues in the field of in-sensor computing. This is the first study to develop a neuromorphic perception neuron based on a self-assembled peptide NW memristor that can encode humidity signals for spiking activity. The spiking characteristics of the newly proposed humidity-perception neuron can be effectively modulated to imitate the strength-modulated spike frequencies in biological neurons. Therefore, it can be integrated into a three-layer SNN as an input unit, which exhibits a high accuracy (92.68%) in lung-disease diagnosis. Owing to the availability of a vast library of peptides and diverse assembly strategies, the proposed strategy could guide diverse research. Tailoring the electrical characteristics and morphology of peptides can enhance the switching energy, endurance, mechanical flexibility, and state differentiation of peptide-based systems. This study could facilitate the design of systems based on self-assembling peptide crystals, which enable the development of a vast repertoire of nanostructures with tunable material properties and are emerging as compelling candidates for unifying sensing, memory, and processing functionalities into neuromorphic devices.

9. Experimental Section

Synthesis of c-YY and c-FF NWs: First, c-YY (or c-FF) powder (10 mg, ≥95%, Bachem) was dissolved in 300 µL of 1,1,1,3,3,3-hexafluor-2-propanol (Sigma-Aldrich, ≥99%) to prepare a c-YY (or c-FF) peptide solution. Subsequently, 1200 µL of H_2O was added into this solution. To fabricate c-YY (or c-FF) NWs, 50 µL freshly prepared c-YY (or c-FF) peptide solution was drop-casted onto a SiO_2 (300 nm)/Si substrate (20 × 20 mm^2) and annealed at 50 °C overnight.

Planar Device (Ag/c-YY NW/Ag) Fabrication: Figure S1 (Supporting Information) shows the fabrication process of Ag/c-YY NW/Ag cells. The SiO_2 (300 nm)/Si substrates were pre-cleaned in absolute ethyl alcohol and deionized water (successively) in an ultrasonic bath for 15 min each and blow-dried with nitrogen before use. Electrodes for the conventional devices were fabricated using ultraviolet lithography technology with a spacing of 2 µm, whereas those for the scaled devices were designed using electron beam lithography patterning with a spacing of 500 nm. Subsequently, a thermal evaporator (Cr/Ag: 5/50 nm) and lift-off procedure were used for electrode fabrication. Next, the c-YY NWs were lifted with a PDMS stamp and transferred onto Ag electrodes using a dry-transfer approach. The Ag/c-FF NW/Ag and Ag/c-YY NW/Ag memristors were fabricated using the same process.

Electrical Measurements of Memristors: A probe station with a humidity-controllable chamber (Nikon GDS-HUMD3) and measurement systems (Keithley 4200A-SCS with pulse measure units and Keysight B2902A) was used for all room-temperature electrical measurements. A

Keithley 4200A-SCS system in the voltage-sweep mode was used for measuring the DC electrical characteristics. During the pulse measurements, a Keysight B2902A system was used as the pulse generator and the output characteristics were monitored. A current compliance of 0.1 mA was used to avoid permanent damage to the device.

In Situ EFM Measurements: The HRS-to-LRS switching process of the Ag/c-YY NW/Ag cell was monitored using an AFM system (Dimension Icon, Bruker) connected to a Keysight B2902A parameter analyzer. AFM topography and phase images were recorded in the tapping and lift modes, respectively, using Bruker EFM tips (SCM-PIT-V2, f_0: 75 kHz, k: 3 N m^{-1}, conductive material: Pt/Ir). The phase image was recorded by positioning the tip ≈100 nm above the sample (scan rate: 1 Hz). The Ag/c-YY NW/Ag cell was connected to a Keysight B2902A instrument via a narrow Cu tape and stimulated at different constant voltages (0, 0.3, and 0.5 V). All AFM measurements were conducted at room temperature and ≈50% RH.

MD Simulations: MD simulations were used to assess the self-assembled structure of c-YY and Ag^+ migration on the c-YY NW surface under 30% and 90% RH. MD simulations using the GROMACS package (2018.4) and a GAFF/TiP3P combination of force fields under stationary temperature/pressure and periodic boundary conditions were used to investigate the self-assembled structure of the c-YY cluster. All hydrogen bonds were restricted during simulations using the LINCS algorithm (integral step: 2 fs). Electrostatic interactions were calculated using the particle mesh Ewald algorithm (cutoff: 10 Å) and updated every ten steps; a constant temperature and pressure of 298.15 K and 1 bar, respectively, was maintained using V-rescale thermostats and the Parrinello–Rahman method. First, the steepest descent method was used to minimize the energy of the system and avoid close contact between atoms followed by 100-ps NVT and NPT equilibrium simulations at 298.15 K. Finally, 50 ns MD simulations were generated under 30% and 90% RH and the conformation of the c-YY cluster was saved every 10 ps. The simulation results were visualized using the GROMACS-embedded program and the VMD software. To assess the Ag^+ migration on the c-YY NW surface, ten Ag cations were introduced into the c-YY cluster and a constant electric field (1.5×10^5 V m^{-1}) was used to drive Ag^+-ion migration. The remaining simulations followed the above-mentioned procedures.

Informed Consent Statement: Human respiration was simulated by controlling a mini humidifier and no human subjects were involved.

Supporting Information

Supporting Information is available from the Wiley Online Library or from the author.

Acknowledgements

Z.L. and S.Z. contributed equally to this work. This research was supported by the NSFC Program (Grant nos. 62122055, 62104154, 62074104, 61974093, 62304137, and 52373248); by the Guangdong Provincial Department of Science and Technology (Grant nos. 2021A1515012569, 2024A1515010006, and 2024A1515011718); by the Science and Technology Innovation Commission of Shenzhen (Grant nos. JCYJ20230808105900001, JCYJ20210324095207020, RCYX20200714114524157, JCYJ20220818100206013, JCYJ20220531102214032, 20231123155543001, and 20200804172625001).

Conflict of Interest

The authors declare no conflict of interest.

Data Availability Statement

The data that support the findings of this study are available from the corresponding author upon reasonable request.

Keywords

artificial neuron, humidity-dependent modulation, neuromorphic perception, peptide memristor, self-assembled nanowire

Received: April 10, 2024
Revised: June 11, 2024
Published online: June 26, 2024

[1] W. J. Laursen, G. Budelli, R. Tang, E. C. Chang, R. Busby, S. Shankar, R. Gerber, C. Greppi, R. Albuquerque, P. A. Garrity, *Neuron* **2023**, *111*, 874.
[2] S. Li, Y. Zhang, X. Liang, H. Wang, H. Lu, M. Zhu, H. Wang, M. Zhang, X. Qiu, Y. Song, Y. Zhang, *Nat Commun* **2022**, *13*, 5416.
[3] P. Guo, B. Tian, J. Liang, X. Yang, G. Tang, Q. Li, Q. Liu, K. Zheng, X. Chen, W. Wu, *Adv Mater* **2023**, *35*, 2304420.
[4] Y. Fang, J. Xu, X. Xiao, Y. Zou, X. Zhao, Y. Zhou, J. Chen, *Adv Mater* **2022**, *34*, 2200252.
[5] Y. Lu, G. Yang, Y. Shen, H. Yang, K. Xu, *Nano-Micro Lett* **2022**, *14*, 150.
[6] Y. Yi, C. Yu, H. Zhai, L. Jin, D. Cheng, Y. Lu, Z. Chen, L. Xu, J. Li, Q. Song, P. Yue, Z. Liu, Y. Li, *Nano Energy* **2022**, *103*, 107780.
[7] B. Loveridge, P. West, N. R. Anthonisen, M. H. Kryger, *Am Rev Respir Dis* **1984**, *5*, 130.
[8] M. J. Tobin, T. S. Chadha, G. Jenouri, S. J. Birch, H. B. Gazeroglu, M. A. Sackner, *Chest* **1983**, *84*, 286.
[9] T. Tiang, Y. Wang, Y. Zheng, L. Wang, X. He, L. Li, Y. Deng, H. Dong, H. Tian, Y. Geng, L. Xie, Y. Lei, H. Ling, D. Ji, W. Hu, *Nat Commun* **2023**, *14*, 2281.
[10] A. Enjin, *Curr Opin Insect Sci* **2017**, *24*, 1.
[11] S. Li, B. Li, L. Gao, J. Wang, Z. Yan, *Nat Commun* **2022**, *13*, 3814.
[12] C. Jiang, J. Liu, Y. Ni, S. Qu, L. Liu, Y. Li, L. Yang, W. Xu, *Nat Commun* **2023**, *14*, 1344.
[13] J. Chen, Z. Zhou, B. J. Kim, Y. Zhou, Z. Wang, T. Wan, J. Yan, J. Kang, J.-H. Ahn, Y. Chai, *Nat Nanotechnol* **2023**, *18*, 882.
[14] H. Jang, H. Hinton, W.-B. Jung, M.-H. Lee, C. Kim, M. Park, S.-K. Lee, S. Park, D. Ham, *Nat Electron* **2022**, *5*, 519.
[15] D. Kwak, D. K. Polyushkin, T. Mueller, *Nat Commun* **2023**, *14*, 4264.
[16] Y. Liu, D. Liu, C. Gao, X. Zhang, R. Yu, X. Wang, E. Li, Y. Hu, T. Guo, H. Chen, *Nat Commun* **2022**, *13*, 7917.
[17] N. Kumar, T. T. Nguyen, J. Lee, M. Patel, P. Bhatnagar, K. Lee, J. Kim, *Adv Sci* **2024**, *11*, 2306408.
[18] S. Wang, X. Chen, C. Zhao, Y. Kong, B. Lin, Y. Wu, Z. Bi, Z. Xuan, T. Li, Y. Li, W. Zhang, E. Ma, Z. Wang, W. Ma, *Nat Electron* **2023**, *6*, 281.
[19] C. Zhang, M. Chen, Y. Pan, Y. Li, K. Wang, J. Yuan, Y. Sun, Q. Zhang, *Adv Sci* **2023**, *10*, 2207229.
[20] S. Zhu, T. Xie, Z. Lv, Y.-B. Leng, Y.-Q. Zhang, R. Xu, J. Qin, Y. Zhou, V. A. L. Roy, S.-T. Han, *Adv Mater* **2023**, *36*, 2301986.
[21] G. Wu, X. Zhang, G. Feng, J. Wang, K. Zhou, J. Zeng, D. Dong, F. Zhu, C. Yang, X. Zhao, D. Gong, M. Zhang, B. Tian, C. Duan, Q. Liu, J. Wang, J. Chu, M. Liu, *Nat Mater* **2023**, *22*, 1499.
[22] M. Lanza, A. Sebastian, W. D. Lu, M. L. Gallo, M.-F. Chang, D. Akinwande, F. M. Puglisi, H. N. Alshareef, M. Liu, J. B. Roldan, *Science* **2022**, *376*, eabj9979.
[23] W. Wang, L. Danial, Y. Li, E. Herbelin, E. Pikhay, Y. Roizin, B. Hoffer, Z. Wang, S. Kvatinsky, *Nat Electron* **2022**, *5*, 870.
[24] L. Pi, P. Wang, S.-J. Liang, P. Luo, H. Wang, D. Li, Z. Li, P. Chen, X. Zhou, F. Miao, T. Zhai, *Nat Electron* **2022**, *5*, 248.
[25] P.-Y. Huang, B.-Y. Jiang, H.-J. Chen, J.-Y. Xu, K. Wang, C.-Y. Zhu, X.-Y. Hu, D. Li, L. Zhen, F.-C. Zhou, J.-K. Qin, C.-Y. Xu, *Nat Commun* **2023**, *14*, 6736.

[26] Y. Zhou, J. Fu, Z. Chen, F. Zhuge, Y. Wang, J. Yan, S. Ma, L. Xu, H. Yuan, M. Chan, X. Miao, Y. He, Y. Chai, *Nat Electron* **2023**, *6*, 870.
[27] X. Pan, J. Shi, P. Wang, S. Wang, C. Pan, W. Yu, B. Cheng, S.-J. Liang, F. Miao, *Sci Adv* **2023**, *9*, eadi4083.
[28] M. Rao, H. Tang, J. Wu, W. Song, M. Zhang, W. Yin, Y. Zhuo, F. Kiani, B. Chen, X. Jiang, H. Liu, H.-Y. Chen, R. Midya, F. Ye, H. Jiang, Z. Wang, M. Wu, M. Hu, H. Wang, Q. Xia, N. Ge, J. Li, J. J. Yang, *Nature* **2023**, *615*, 823.
[29] Y. Ren, X. Bu, M. Wang, Y. Gong, J. Wang, Y. Yang, G. Li, M. Zhang, Y. Zhou, S.-T. Han, *Nat Commun* **2022**, *13*, 5585.
[30] I.-J. Kim, M.-K. Kim, J.-S. Lee, *Nat Commun* **2023**, *14*, 504.
[31] S. Wang, Y. Li, D. Wang, W. Zhang, X. Chen, D. Dong, S. Wang, X. Zhang, P. Lin, C. Gallicchio, X. Xu, Q. Liu, K.-T. Cheng, Z. Wang, D. Shang, M. Liu, *Nat Mach Intell* **2023**, *5*, 104.
[32] Z. Zhang, X. Zhao, X. Zhang, X. Hou, X. Ma, S. Tang, Y. Zhang, G. Xu, Q. Liu, S. Long, *Nat Commun* **2022**, *13*, 6590.
[33] K. Liu, C. Wang, B. Liu, Y. Bian, J. Kuang, Y. Hou, Z. Pan, G. Liu, X. Huang, Z. Zhu, M. Qin, Z. Zhao, C. Jiang, Y. Liu, Y. Guo, *Adv Mater* **2023**, *35*, 2207006.
[34] Y. Du, J. Tang, Y. Li, Y. Xi, Y. Li, J. Li, H. Huang, Q. Qin, Q. Zhang, B. Gao, N. Deng, H. Qian, H. Wu, *Adv Mater* **2023**, *36*, 2302658.
[35] S. Kumar, X. Wang, J. P. Strachan, Y. Yang, W. D. Lu, *Nat Rev Mater* **2022**, *7*, 575.
[36] K. He, C. Wang, Y. He, J. Su, X. Chen, *Chem Rev* **2023**, *123*, 13796.
[37] G. S. Syed, Y. Zhou, J. Warner, H. Bhaskaran, *Nat Nanotechnol* **2023**, *18*, 1036.
[38] T. Fu, X. Liu, H. Gao, J. E. Ward, X. Liu, B. Yin, Z. Wang, Y. Zhuo, D. J. F. Walker, J. J. Yang, J. Chen, D. R. Lovley, J. Yao, *Nat Commun* **2020**, *11*, 1861.
[39] Y. Zhang, L. Liu, B. Tu, B. Cui, J. Guo, X. Zhao, J. Wang, Y. Yan, *Nat Commun* **2023**, *14*, 247.
[40] M.-K. Song, S. D. Namgung, D. Choi, H. Kim, H. Seo, M. Ju, Y. H. Lee, T. Sung, Y.-S. Lee, K. T. Nam, J.-Y. Kwon, *Nat Commun* **2020**, *11*, 5896.
[41] Z. Lv, X. Xing, S. Huang, Y. Wang, Z. Chen, Y. Gong, Y. Zhou, S.-T. Han, *Matter* **2021**, *4*, 1702.
[42] H. Shi, R. Wang, P. Yu, J. Shi, L. Liu, *Appl Nanosci* **2021**, *11*, 961.
[43] F. Wang, F. Hu, M. Dai, S. Zhu, F. Sun, R. Duan, C. Wang, J. Han, W. Deng, W. Chen, M. Ye, S. Han, B. Qiang, Y. Jin, Y. Chua, N. Chi, S. Yu, D. Nam, S. H. Chae, Z. Liu, Q. J. Wang, *Nat Commun* **2023**, *14*, 1938.
[44] F. Ye, F. Kiani, Y. Huang, Q. Xia, *Adv Mater* **2023**, *35*, 2204778.
[45] T. Wang, J. Meng, X. Zhou, Y. Liu, Z. He, Q. Han, Q. Li, J. Yu, Z. Li, Y. Liu, H. Zhu, Q. Sun, D. W. Zhang, P. Chen, H. Peng, L. Chen, *Nat Commun* **2022**, *13*, 7432.
[46] D. Kireev, S. Liu, H. Jin, T. P. Xiao, C. H. Bennett, D. Akinwande, J. A. C. Incorvia, *Nat Commun* **2022**, *13*, 4386.
[47] S. Tappertzhofen, M. Hempel, I. Valov, R. Waser, *Mater Res Soc Symp Proc* **2011**, *1330*, 302.
[48] S. G. Sarwat, T. Moraitis, C. D. Wright, H. Bhaskaran, *Nat Commun* **2022**, *13*, 2247.
[49] Q. Wang, Y. Park, W. D. Lu, *Adv Intell Syst* **2022**, *4*, 2100199.
[50] S. Liu, J. Zeng, Z. Wu, H. Hu, A. Xu, X. Huang, W. Chen, Q. Chen, Z. Yu, Y. Zhao, R. Wang, T. Han, C. Li, P. Gao, H. Kim, S. J. Baik, R. Zhang, Z. Zhang, P. Zhou, G. Liu, *Nat Commun* **2023**, *14*, 7655.
[51] H. Shi, M. Li, J. Shi, D. Zhang, Z. Fan, M. Zhang, L. Liu, *ACS Appl Mater Interfaces* **2021**, *13*, 1057.
[52] A. Choter-Ouda, A. Jeziorna, S. Kaźmierski, R. Dolot, M. K. Dudek, M. J. Potrzebowski, *Phys. Chem. Glasses: Eur. J. Glass Sci. Technol., Part B* **2022**, *28*, 202202005.
[53] S. Chen, M. R. Mahmoodi, Y. Shi, C. Mahata, B. Yuan, X. Liang, C. Wen, F. Hui, D. Akinwande, D. B. Strukov, M. Lanza, *Nat Electron* **2020**, *3*, 638.
[54] W. Sun, B. Gao, M. Chi, Q. Xia, J. J. Yang, H. Qian, H. Wu, *Nat Commun* **2019**, *10*, 3453.
[55] H. Kim, M. R. Mahmoodi, H. Nili, D. B. Strukov, *Nat Commun* **2021**, *12*, 5198.
[56] X. Huang, C. Liu, Z. Tang, S. Zeng, S. Wang, P. Zhou, *Nat Nanotechnol* **2023**, *18*, 486.
[57] Y. Wang, Y. Gong, S. Huang, X. Xing, Z. Lv, J. Wang, J.-Q. Yang, G. Zhang, Y. Zhou, S.-T. Han, *Nat Commun* **2021**, *12*, 5979.
[58] K. Liu, T. Zhang, B. Dang, L. Bao, L. Xu, C. Cheng, Z. Yang, R. Huang, Y. Yang, *Nat Electron* **2022**, *5*, 761.
[59] Y. Yang, X. Zhang, L. Qin, Q. Zeng, X. Qiu, R. Huang, *Nat Commun* **2017**, *8*, 15173.
[60] G. Milano, F. Raffone, M. Luebben, L. Boarino, G. Cicero, I. Valov, C. Ricciardi, *ACS Appl Mater Interfaces* **2020**, *12*, 48773.
[61] T. Tsuruoka, K. Terabe, T. Hasegawa, I. Valov, R. Waser, M. Aono, *Adv Funct Mater* **2012**, *22*, 70.
[62] R. Yuan, Q. Duan, P. J. Tiw, G. Li, Z. Xiao, Z. Jing, K. Yang, C. Liu, C. Ge, R. Huang, Y. Yang, *Nat Commun* **2022**, *13*, 3973.